Published in final edited form as:
J Bone Miner Res. 2014 April ; 29(4): 878–891. doi:10.1002/jbmr.2105.

Perlecan-containing pericellular matrix regulates solute transport and mechanosensing within the osteocyte lacunar-canalicular system

Bin Wang[1,2,*], **Xiaohan Lai**[1,*], **Christopher Price**[1], **William R. Thompson**[3], **Wen Li**[1], **Tonima R. Quabili**[1], **Wei-Ju Tseng**[4], **Xiaowei Sherry Liu**[4], **Hong Zhang**[5], **Jun Pan**[2], **Catherine B. Kirn-Safran**[6], **Mary C. Farach-Carson**[7], and **Liyun Wang**[1,#]

Bin Wang: waybing@gmail.com; Xiaohan Lai: laixhan@udel.edu; Christopher Price: cprice@udel.edu; William R. Thompson: wthomp@med.unc.edu; Wen Li: wenli@udel.edu; Tonima R. Quabili: tonima.quabili@gmail.com; Wei-Ju Tseng: weijut@gmail.com; Xiaowei Sherry Liu: xiaoweil@mail.med.upenn.edu; Hong Zhang: zhang@rowan.edu; Jun Pan: panj@cqu.edu.cn; Catherine B. Kirn-Safran: ckirn@udel.edu; Mary C. Farach-Carson: farachca@rice.edu; Liyun Wang: lywang@udel.edu

[1]Department of Mechanical Engineering, University of Delaware, Newark, DE 19716, USA

[2]Key Laboratory for Biorheological Science and Technology of Ministry of Education, Bioengineering College, Chongqing University, Chongqing 400044, PR China

[3]Department of Medicine, University of North Carolina, Chapel Hill, NC 27599, USA

[4]McKay Orthopedic Research Laboratory, Department of Orthopedic Surgery, University of Pennsylvania, Philadelphia, PA 19104, USA

[5]Department of Mechanical Engineering, Rowan University, Glassboro, NJ 08028, USA

[6]Department of Biological Sciences, University of Delaware, Newark, DE 19716, USA

[7]Department of Biochemistry and Cell Biology, Rice University, P.O. Box 1892, MS-140, Houston, TX 77251, USA

Abstract

The pericellular matrix (PCM), a thin “coating” surrounding nearly all mammalian cells, plays a critical role in many cell-surface phenomena. In osteocytes, the PCM is believed to control both “outside-in” (mechanosensing) and “inside-out” (signaling molecule transport) processes. However, the osteocytic PCM is challenging to study *in situ* because it is thin (~100nm) and enclosed in mineralized matrix. To this end, we recently developed a novel tracer velocimetry approach that combined fluorescence recovery after photobleaching (FRAP) imaging with hydrodynamic modeling to quantify the osteocytic PCM in young murine bone (Wang et al., J Bone Miner Res. 2013; 28:1075–86). In this study, we applied the technique to older mice expressing or deficient for perlecan/HSPG2, a large heparan-sulfate proteoglycan normally secreted in osteocytic PCM. The objectives were to i) characterize transport within an altered PCM; ii) to test the sensitivity of our approach in detecting the PCM alterations; and iii) to dissect the roles of the PCM in osteocyte mechanosensing. We found that i) solute transport increases in

[#]Corresponding author: Liyun Wang, Ph.D., Center for Biomedical Engineering Research, Department of Mechanical Engineering, 130 Academy Street Newark, DE 19716, Tel: 302.831.2659, Fax: 302.831.3619, lywang@udel.edu.
[*] The first two authors contributed equally to this work

Disclosures: All authors state that they have no conflicts of interest.

Author contributions: Study design—LW and CP; Data collection--BW, CP and WL for FRAP experimental data, XL and LW for modeling, XL, TB, WT, XSL, HZ and CP for in vivo loading study; Data and statistical analysis-- BW, XL, TB, WT, CP and LW; Data interpretation and manuscript drafting-- BW, XL, CP, and LW; Manuscript revising—all authors. LW takes responsibility for the integrity of the study.

the perlecan-deficient (hypomorphic: Hypo) mice compared with control mice; ii) PCM fiber density decreases with aging and perlecan deficiency; iii) the osteocytes in the Hypo bones are predicted to experience higher shear stress (+34%), but decreased fluid drag force (−35%) under 3N peak tibial loading, and iv) when subjected to tibial loading in a preliminary *in vivo* experiment, the Hypo mice did not respond to the anabolic stimuli as CTL mice. These findings support the hypothesis that the PCM fibers act as osteocyte's sensing antennae, regulating load-induced cellular stimulations and thus bone's sensitivity and *in vivo* bone adaptation. If this hypothesis is further confirmed, osteocytic PCM could be new targets to develop osteoporosis treatments by modulating bone's intrinsic sensitivity to mechanical loading and be used to design patient-specific exercise regimens to promote bone formation.

Keywords

Pericellular Matrix; Perlecan Deficiency; HSPG2; Fluid Drag Force; Mechanosensing

Introduction

Osteocytes, the most numerous cells in bone, play a central role in maintaining tissue homeostasis (1) and sensing the mechanical stimuli that drive bone adaptation (2). A fibrous, non-mineralized pericellular matrix (PCM) has been found to surround the osteocytes and their long "dendritic" processes within the lacunar-canalicular pore system (LCS) (3). This thin cellular "coating," also termed the glycocalyx, is a universal structure, found in nearly all mammalian cells such as red blood cells (4), endothelial cells (5), epithelial cells (6), and chondrocytes (7). As an interface between cell membrane and extracellular space, the PCM is essential for cell surface phenomena such as cell-cell, cell-ligand, and cell-extracellular matrix (ECM) interactions (4,5). In particular, the PCM's mechanosensitive function is well established in endothelial cells (5,8) and chondrocytes (9,10). Two *in vitro* findings that disrupting the PCM of osteocytic MLO-Y4 cells completely abolished flow-induced PGE2 release and the opening of the connexin 43 hemichannels highlight the functional importance of the PCM in osteocyte mechanosensing and *in vivo* bone adaptation to mechanical loading.

Being strategically positioned between the cell and its immediate external environment, the PCM is critical during both the "*outside-in*" and "*inside-out*" signaling processes that occur in and among osteocytes. Under dynamic loading, the porous bone matrix is deformed and the interstitial fluid is driven to flow through the LCS pores (11,12), where the PCM fibers fill the annular space between the canalicular wall and the cell membrane (3,13). The magnitude of this load-induced fluid flow and its relaxation time constant are highly dependent on the hydraulic permeability of the LCS pores, which scales approximately to the square of the fiber spacing (13). The PCM fibers, therefore, help regulate the "*outside-in*" process, whereby the tissue-level mechanical loads are converted into cellular stimulations. Among several proposed mechanisms by which the whole-bone level external loading can be perceived at the cellular level (14), two of the most commonly accepted involve fluid-fiber interactions. One is through the action of fluid shear stress on the cell membrane, in which the PCM fibers control the fluid velocity profiles in the canaliculi and determines the magnitude of the fluid shear stress (13); the other is through the direct drag forces on the PCM fibers (15). Although both loading signals result from fluid flow, shear stress describes the interactions between the flow and cell membrane surface (unit: Pa) and the fluid drag force indicates the normal force that fluid flow impacts on the transverse PCM fibers (unit: N). Both physical signals could be transmitted to the cell's interior via apparati such as focal adhesion complexes (16,17), stretch activated membrane channels (18), voltage sensitive channels (19), or the cytoskeleton (15). Once activated by mechanical

stimuli, osteocytes can alter the expression of various signaling molecules that can subsequently orchestrate the activities of osteoblasts, osteoclasts, and other functional cells, fostering bone's adaptation to mechanical environment (2). During this signaling process, termed "*inside-out*", the osteocyte PCM serves as an important molecular sieve, controlling the passage and final presentation of signaling molecules within bone (20–22). Therefore, *alterations* in PCM structure and composition are expected to impact both osteocyte's sensing and responses to mechanical loading at multiple levels.

Despite its potential significance in bone physiology, our current knowledge of the osteocytic PCM and its alterations *in vivo* remains limited because of the lack of quantitative measurement tools. The existence of fibrous PCM in adult bone has been demonstrated in transmission electron microscopy (TEM) since the 1990s (23,24). Utilizing fixatives containing ruthenium III hexamine trichloride, a cationic dye previously used to stain cartilage proteoglycan (25) and the endothelial glycocalyx (26), You et al. (2004) identified transverse tethering fibers spanning the entire annular fluid space (3), the essential force-transferring element for a proposed strain amplification mechanism (15). In our recent study, perlecan/HSPG2, a large secreted heparan sulfate proteoglycan, was discovered within the osteocytic PCM under immunofluorescence and TEM immunogold staining methods (27). The importance of perlecan in the osteocytic PCM was further confirmed by TEM imaging of the osteocytic LCS from C1532Yneo mice (27), a transgenic model developed to recapitulate the reduced perlecan expression associated with Schwartz-Jampel Syndrome (SJS) (28) and derived by us on a C57BL/6J genetic background. These perlecan-deficient (hypomorph: Hypo) mice exhibited a significant decrease in perlecan secretion (28), and decreased number of tethering elements per canaliculus (−35.8%) in our recent TEM study (27). In non-mineralized tissues such as the kidney, decreased expression of heparan sulfate was reported to be associated with marked edema and proteinuria, suggesting an elevated glomerular permeability to solutes (29). However, it is not known if the hydraulic permeability and load-induced solute transport are altered within the bone LCS of the perlecan-deficient mice.

Although the TEM technique is useful to study morphology and composition of the osteocytic PCM, quantitative measurements of PCM fiber density based on TEM remain a challenge because i) the PCM fibers are fragile and easily collapsible (5) and ii) the TEM histological procedures are tedious and prone to artifacts (26). To this end, we recently developed a novel *in situ* approach to quantify PCM fiber density based on tracer velocimetry, which combined confocal fluorescence recovery after photobleaching (FRAP) imaging and hydrodynamic modeling (30). Using this technique we successfully measured, for the first time, the osteocytic PCM fiber density of bone from young adult mice *in situ* (30). It was not clear from that study if the tracer velocimetry approach would be sensitive enough to detect PCM alterations that may occur *in vivo* and their possible impacts on osteocyte mechanobiology.

The goal of the present investigation was four-fold. First, we aimed to quantify changes in molecular diffusion and convection in the cortical bone of the perlecan-deficient mice relative to controls. We hypothesized that the perlecan deficiency would increase solute transport in the bone LCS due to reduced hydraulic resistance from the PCM. Second, using older perlecan-deficient and age-matched perlecan-expressing control mice, we tested the sensitivity of our tracer velocimetric FRAP approach in detecting PCM alterations associated with aging and perlecan deficiency. Third, the cellular-level stimulating forces (shear stress *vs.* fluid drag) were estimated from the PCM structure using the Brinkman equation describing fluid flow in a porous medium (13), and last, we correlated mechanical stimulations at the cellular level with bone's responses to *in vivo* tibial loading. Our preliminary results suggest that the fluid drag force acting on the PCM fibers is the primary

physical signal driving bone adaptation and lead us to hypothesize that the proteoglycan perlecan in PCM, acting as flow-sensing antenna on osteocytes, regulates bone's sensitivity to mechanical loading. If this hypothesis is further confirmed in future in vivo studies, quantification of the PCM fiber density or related characteristics could be a powerful tool to identify individual's sensitivity to loading, allowing design patient-specific exercise regimens, or to provide new targets to promote bone formation in osteoporotic patients, enabling the modulation of bone's intrinsic sensitivity to mechanical loading.

Methods

Mice

Mice with perlecan deficiency, a generous gift from Dr. Kathryn Rodgers, were used in this study. The generation and characterization of this murine model of human Schwartz-Jampel Syndrome (SJS) (31) were published previously (28). Disruption of the functional perlecan gene expression was achieved by retention of a neomycin selection cassette (C1532Yneo) on intron 16 located between exons encoding for perlecan, resulting in a decreased perlecan secretion in homozygous mutants (28). These mice were referred to as hypomorphic (Hypo) owing to the reduced perlecan expression but a less severe phenotype than a lethal null condition (32). Wild-type animals and those heterozygous for the C1532Yneo mutation were undistinguishable phenotypically, and both were used as controls (CTL) (28). All animal studies were performed with the approval of the Institutional Animal Care and Use Committee (IACUC) of the University of Delaware.

Tibial Compliance Measurements

Prior to the tracer velocimetry FRAP tests, which required application of comparable surface strains to the Hypo and CTL tibiae, the compliances of the tibiae were quantified in 8–9 month-old male Hypo (n=7) and CTL (n=4) tibiae using the optical strain measurement method described previously (33). The tibiae were painted with fluorescent microspheres and subjected to incrementally increased loads, while axial strain was quantified at the anterior-medial surface (25–50% distal of the proximal end) using a digital image correlation algorithm. The mean compliance of the tibiae was obtained by linearly fitting the strain versus load curves. Because no significant difference was detected in the compliance of the tibiae between the two genotypes, a 3N peak load was applied to both genotypes during the FRAP tests described later.

Quantification of the LCS Anatomy

In a separate set of 8–9 month-old male Hypo and CTL mice (n=3 mice/genotype), right tibiae were harvested and immediately immersed in chemical fixatives containing ruthenium III hexamine trichloride in preparation for TEM imaging (3). High-resolution TEM images were analyzed using the previously described protocol (27). The total canalicular area, cell process area, and the pericellular fluid area were obtained from the TEM images of the canalicular cross-sections (n=506 and 475 canaliculi) for the CTL and Hypo groups, respectively. In addition, the gap in the peri-lacunar fluid area between the cell membrane and lacunar wall was measured in 12 and 16 lacunae for the CTL and Hypo cortical bones, respectively. The left tibiae were fixed, bulk stained with basic fuchsin and embedded in methyl methacrylate, followed by sagittal sectioning and polishing to a thickness of 100μm (34). A total of 30 intact lacunae per genotype (10 lacunae per mouse) were randomly selected from the tibial cortical bone compartment and imaged using a Zeiss LSM510 confocal microscope. Z-stack images were obtained with a z-step of 0.2 μm using an oil-immersion lens (40×). Three-dimensional reconstructions were performed using the Volocity® software package (PerkinElmer, Waltham, MA) and the number of canaliculi emanating from each lacuna was counted. The lacunar bodies were segmented in the

Amira® software package (Visualization Sciences Group, Burlington, MA) and their surface areas and volumes were calculated. An axial correction factor (0.803), which was determined optically using calibrated bone sections with known thicknesses, was applied to correct the axial stretching of images (35). The canalicular number density per unit surface area was determined for each genotype. These anatomical measurements were used in calculating tracer diffusivity and customizing genotype-specific LCS models to derive solute velocities as detailed below.

FRAP Specimen Preparation

12–13 month-old male Hypo (n=7) and CTL (n=5) mice were used in this study. These relatively older mice were chosen i) to match our previous TEM studies where the LCS anatomical parameters were characterized in 8–9 month-old male mice and ii) to allow comparison between aged and young adult bones, which were investigated in our previous PCM studies (30). The mice were injected via the tail vein with 0.5mL of phosphate buffered saline (PBS) containing either 5 mg sodium fluorescein (Sigma-Aldrich, St. Louis, MO) or 2 mg parvalbumin conjugated with Alexa Fluor 488 (Molecular Probes/Invitrogen Corp., Carlsbad, CA), as described previously (30). Out of a total of twelve mice, two CTL and five Hypo mice received sodium fluorescein and three CTL and two Hypo mice received parvalbumin. We used both tibiae and imaged multiple lacunae per animal to increase our detection power. The two tracers (molecular weights: 376Da and 12.3kDa) were chosen because they represented a small and a relatively large molecule in the broad spectrum of nutrients, metabolites, and signaling molecules involved in osteocyte function (2,22). The tracers were allowed to circulate for 0.5h and 2h in alert and mobile mice, respectively, prior to sacrifice (22). The left tibia then was harvested, cleansed of soft/adherent tissues, and tested within 0.5–3h *post-mortem*. The right contralateral tibiae were immediately frozen, stored, and then thawed prior to testing at a later date.

FRAP Tracer Velocimetry

To obtain measures of the osteocytic PCM's fiber density such as the fiber volume fraction and the fiber spacing, a three-step procedure was developed (30), including i) quantification of solute transport using FRAP tests, ii) quantification of solute velocity using the three-compartment LCS transport simulations, and iii) estimation of the PCM fiber density based on the hydrodynamic sieving modeling. Each step is detailed below.

Step #1: Quantify solute transport using FRAP tests—As described previously (12), our experimental set-up consisted of an electromagnetically actuated loading device (Electroforce LM1 TestBench, Bose Corporation, Eden Prairie, MN) integrated with an inverted confocal laser-scanning microscope (Zeiss LSM 510, Carl Zeiss Inc., Thornwood, NY). A 40×, 0.8 numerical aperture water dipping lens attached to an objective inverter was used to capture images of tibia, which was held in a PBS bath maintained at 37°C. A typical FRAP procedure consisted of three phases of imaging (pre-bleach, photobleaching, and recovery) (12,34) of fluorescently labeled lacunae approximately 25–40μm below the tibial periosteal surface on the anterior-medial surface ~25% to 50% distal from the proximal tibial plateau. The imaging settings include 488nm excitation, 505–530nm emission, 512×512-pixel images, scanning speed of ~1s/frame, and a pinhole of ~4.2–6.4 Airy unit. We subjected the same lacuna to two sequential FRAP trials: the first was a convection test under cyclic loads (3.0N peak load at 0.5 Hz) and the second was a diffusion test under the tare load (0.2N). A 4sec resting period was inserted between the two adjacent loading cycles during convection tests to minimize motion artifacts during imaging (12).

The outcomes from this step included the transport rates of the two tracers during diffusion and convection tests, as well as the diffusivity and the transport enhancement for each tracer.

The specific methods in obtaining these measures from the FRAP and anatomical data were published previously (12,34). The transport rate, the reciprocal of the characteristic time constant of the exponential recovery of the fluorescence, were obtained directly from the FRAP image series (34). Tracer diffusivity was then derived from the diffusion FRAP tests (34). In parallel, the transport enhancements (k/k_0), the ratio of the transport rate under loading over that under static condition, were obtained from paired FRAP tests using each tracer (12,30).

Step #2: Quantify tracer velocity using LCS transport simulations—Because the anatomical features of the transport source (*i.e.*, surrounding lacunae), transport sink (*i.e.*, photobleached lacuna), and the connecting channels are known, the flow velocity in individual canaliculus could be readily back calculated from the transport enhancement data by simulating the diffusion and convection during FRAP tests (12,30). Average anatomical parameters for the lacunae studied (summarized for each genotype in the Results section) were used to customize a three-compartment LCS transport model for each genotype (12,30). The model consisted of three compartments representing the photobleached lacuna (sink) and two neighboring reservoirs that served as alternating upstream and downstream source to the transport sink during cyclic loading (Fig. 2 of reference (12)). Model parameters such as canalicular length, lacunar major and minor radii, and calculated lacunar surface area were obtained from the pre-bleach FRAP images (34); the contributing canalicular number, canalicular annular fluid area, and the extracellular fluid area around lacunae were obtained in the preceding section (Quantification of the LCS anatomy) (34). Using the mean diffusivities of sodium fluorescein and parvalbumin in the LCS of the Hypo and CTL bones obtained in the step #1, the temporal concentration profiles within the photobleached lacuna were simulated computationally for any given peak solute velocity (0–80μm/s) (36), from which a relationship between solute convection and transport enhancement (k/k_0) was established (12,30). Thus, the solute velocities corresponding to the observed transport enhancements within the FRAP experiments, v_s, were obtained.

The outcomes from the second step included the reflection coefficients of parvalbumin in the Hypo and CTL bones. The reflection coefficient ($\sigma=1-v_s/v_f$) characterized the hindrance of the velocity of parvalbumin (v_s) relative to that of fluid (v_f) due to steric and hydrodynamic interactions between parvalbumin and the PCM fibers in the LCS. The fluid flow velocity v_f in loaded bone was measured using sodium fluorescein, which has a small Stokes radius (≈0.45nm) and a negligible reflection coefficient (30). These reflection coefficients were measured in aged (12–13 month-old) bone in this study and compared with that of younger (4–5 month old) bone measured previously (30).

Step #3: Quantify osteocytic PCM fiber density using hydrodynamic sieving modeling—PCM configurations, such as the fiber volume fraction and the fiber edge-to-edge spacing in the CTL (12–13 month-old), Hypo (12–13 month-old), and young adult CTL (4–5 month-old) bone, were obtained using our newly developed PCM hydrodynamic sieving model (30). Because the radius of individual fibers in the PCM is unknown, we parametrically varied the fiber radius from 0.5 nm (radius of glycosaminoglycan (GAG) side chains (13)), 1–2nm (radius of perlecan core protein (37)), and 4nm (repeated features of the endothelial glycocalyx (26)). We determined the fiber volume and edge-to-edge fiber spacing of these fibers that accounted for the observed reflection coefficients in the three groups. Because the TEM images showed that within canaliculi fibers arranged dominantly in the radial transverse direction (3,27), a radial square fiber array was assumed in this study. In order to permit comparisons with previous tracer perfusion results, the fiber spacing reported in this paper was the edge-to-edge measure. The relationship between the fiber volume fraction (k_{vf}) and the edge-to-edge fiber spacing (Δ):

$$kvf = \frac{\pi {r_f}^2}{(\Delta + 2r_f)^2}. \quad \text{(Eq. 1)}$$

The outcomes of the third step included the fiber volume fraction and the fiber edge-to-edge spacing for aged Hypo, aged CTL, and young adult CTL bone.

Cellular-Level Mechanical Stimulations

The peak fluid velocity and the fiber spacing, both measured using the above FRAP tracer velocimetry, were used to obtain detailed spatial velocity profile inside the canaliculi, from which the shear stress on the cell process membrane and the fluid drag force experienced by the PCM transverse fibers were calculated. For fluid flow through a porous media (*i.e.*, the PCM fibers inside the canaliculi), Weinbaum *et al*. (1994) solved the Brinkman equation with non-slip boundary conditions and derived a formula of the fluid velocity as a function of the pressure gradient and the hydraulic permeability of the PCM fibers, which scales approximately to the square of the fiber spacing. We derived the formula for the fluid flux in one canaliculus by integrating the fluid velocity over the entire fluid annulus, with a single unknown factor (the pressure gradient). To resolve the pressure gradients in our loaded bones, we compared the measured fluid flux (the product of fluid velocity and the canalicular fluid annular cross-sectional area) with the predicted fluid flux formula. The detailed fluid velocity profile, shearing force on the cell membrane (13), and the fluid drag force acting on the transverse PCM fibers per unit cell process length (1μm) were therefore obtained as previously reported (15).

In Vivo Tibial Loading

The right tibiae of 3.5-month-old Hypo mice (n=6) and age-matched CTL male mice (n=8) were subjected to compressive uniaxial-tibial loading using a previously published protocol (38) with a peak load 8.5N at 4 Hz (*i.e.*, 0.075s ramp up, 0.075 ramp down, and 0.1s dwell time), 5 min/session, and 5 sessions over 10 days. The peak load magnitude was found to induce similar surface strains (~1300 με) at the FRAP imaging sites in a separate set of Hypo and CTL tibiae (n=4). The left tibiae served as non-loaded control. The mice received intra-peritoneal injections of calcium-binding calcein (30mg/kg) on Day 1 and Day 11 and were sacrificed on Day 15. The 3mm mid-shafts of harvested tibiae were first scanned in a microCT system (μCT35, Scanco Medical AG, Switzerland) with an isotropic voxel size of 6μm (39), subjected to three-point bending test along the anterior-posterior direction with a lower support span of 4.5mm and a loading rate of 0.05mm/s using a TA RSA G2 mechanical analyzer (TA Instruments, New Castle, DE), and then fixed and embedded in methyl methacrylate for dynamic histomorphometry analysis using OsteoMeasure (OsteoMetrics, Inc, Decatur, GA). The μCT-based microstructural parameters were obtained through three-dimensional reconstruction and segmentation (using a Gaussian filter and a global threshold of 4311Hunsfield units) in the manufacturer provided software. The dynamic bone labeling analysis was performed on two mid-diaphyseal cross-sections per bone sample and their average values were used. These parameters were compared between loaded and non-loaded tibiae and between Hypo and CTL mice.

Statistical Analysis

All statistical analyses and regressions were performed using the Prism software package (GraphPad Software, La Jolla, CA). The optically measured strains at various load magnitudes were linearly regressed for all the animals in either Hypo or CTL groups and the difference between the slopes of the two regression lines was detected. The anatomical measures of the studied lacunae, as well as the confocal 3D and TEM imaging data were

analyzed using unpaired, two-tailed Student's *t* tests between the Hypo and CTL groups. The diffusivity and transport enhancement data were analyzed with two-way ANOVA (genotype and tracer type) and Bonferroni's multiple comparison post-hoc tests. Unpaired, two-tailed Student's *t*-tests also were performed when comparing Hypo vs. CTL groups. For the *in vivo* loading data, paired and unpaired two-tailed Student's *t*-tests were used for comparing loaded *vs*. non-loaded tibiae and Hypo *vs.* CTL, respectively. The significance level was set at $p<0.05$ for all statistical tests.

Results

Tibial compliance

To ensure the induction of similar mechanical strains on loaded Hypo and CTL tibiae during the FRAP tests, the compliance of the tibiae under axial compression was measured optically for each group. The following strain-load relationships were found by linear regression:

$$\text{CTL tibiae:Strain}\,(\mu\varepsilon)=101.9\times\text{Load}\,(\text{N})\,(\text{R}^2=0.93,\text{N}=7);\quad \text{(Eq. 2)}$$

$$\text{Hypo tibiae:Strain}\,(\mu\varepsilon)=96.1\times\text{Load}\,(\text{N})\,(\text{R}^2 0.99,\text{N}=4).\quad \text{(Eq. 3)}$$

Due to inter-sample variation, there was no significant difference in the average compliance between CTL and Hypo groups (96.1 *vs.* 101.9 με/N, Fig. 1S). Therefore, a 3N peak cyclic compressive load (*i.e*., 2.8N dynamic magnitude relative to the 0.2N tare load) was applied to all tibiae during the convection FRAP trials.

LCS Anatomy

To quantify solute diffusivity and to construct the three-compartment transport model, the number of canaliculi contributing to tracer recovery during the FRAP tests needed to be quantified, as well as the volume of the canalicular channels connecting to the photobleached lacuna. Using 3D confocal and TEM imaging, we first quantified the number density of the canaliculi emanating from each lacuna as well as the LCS annular fluid cross-sectional area (Table 1). The canalicular number density per unit lacunar surface area was 0.21±0.04 and 0.19±0.02 #/μm^2 for CTL and Hypo lacunae (n=30 for both groups), respectively. The CTL value was not different from that of 4–5-month B6 mice (0.21±0.05 #/μm^2) reported in our earlier studies (34), but was significantly higher than that of the Hypo group ($p<0.05$). Both cross-sectional areas for the canaliculi (bound by the canalicular walls) and the cell processes were significantly reduced in the Hypo bones compared with those in the CTL bones ($p<0.0001$ and $p=0.0002$, respectively), resulting in a decreased canalicular fluid annular area for the Hypo canaliculi (0.053±0.026 μm^2, n=475) versus the CTL ones (0.065±0.034μm^2, n=506). The typical peri-lacunar fluid gap, the space between the cell membrane and lacunar wall, was measured to be 0.47±0.27μm (median 0.40, n=12 lacunae) and 0.38±0.17μm (median 0.35, n=16 lacunae) for CTL and Hypo bone, respectively. Since there was no significance between the two groups ($p=0.32$) the data were pooled and a median value of 0.36μm was used in this study. The genotype-specific canalicular values are listed in Table 1.

Morphologies of Lacunae Subjected to FRAP

For both Hypo and CTL bones 79 lacunae were subjected to FRAP tests (Table 2). The means and standard deviations of their projection area (*A*), calculated lacunar volume (*LacVol*) and surface area *(LacSurf*), contributing canalicular number (*n*) and canalicular

length (*d*), as well as the relative volume ratio between the sink lacuna and the contributing canaliculi *Vr* (*CanVol/LacVol*) are listed in Table 2. The coefficients of variation for these measures were typically between 10% and 30%, but some parameters (*LacVol*) showed the coefficient of variation as high as 50%, indicating significant variations among tested lacunae. Although no significant difference between the two genotypes ($p>0.05$) was detected in the projected area, lacunar volume and surface area, significant differences were found in contributing canalicular number, canalicular length, and the relative volume ratio between the CTL and Hypo groups ($p<0.003$). These parameters measured in the FRAP tests (Table 2) in combination with the TEM data (Table 1) were used to construct the genotype-specific three-compartment LCS transport models.

Tracer Diffusivity

Taking account of each individual lacuna's morphology and its connectivity to surrounding lacunae (34), tracer diffusivity in the LCS demonstrated a clear dependency on the tracer type and genotype using two-way ANOVA analysis (genotype $F_{1,92}=16.4$, $P<0.0001$ and tracer type $F_{1,92}=25.31$, $P<0.0001$) (Fig. 1). The diffusivity of sodium fluorescein increased +33% in the Hypo bones($402\pm126\mu m^2/s$, n=38) compared with the CTL bones ($302\pm72\mu m^2/s$, n=33, $p<0.05$), while that of parvalbumin increased +40% in the Hypo bones ($280\pm61\mu m^2/s$, n=11) compared with the CTL bones ($200\pm55\mu m^2/s$, n=14, $p<0.05$). Between the two tracers, the diffusivity of the larger parvalbumin decreased significantly (−34% and −30% in the CTL and Hypo bones, respectively), compared with that of the smaller tracer sodium fluorescein in bones of the same genotypes ($p<0.05$, compare hatched and solid bars in Fig. 1).

Transport Enhancement

Paired convection/diffusion FRAP tests performed on the same lacunae under both loaded and static conditions allowed measurements of transport enhancement (k/k_0) for both CTL and Hypo bones (Fig. 2). Two-way ANOVA showed that genotype ($F_{1,56}=4.44$, $p=0.04$) and tracer type ($F_{1,56}=8.08$, $p=0.006$) had significant effects on the transport enhancement. Due to the small sample size, the Bonferroni multiple comparison tests did not detect any significant difference between the group means. However, by Student's *t*-test the transport enhancement of sodium fluorescein increased marginally (+6%, $p=0.17$) in the Hypo bones (1.26±0.14, n=16) compared with the CTL bones (1.19±0.15, n=20) while that of parvalbumin increased significantly (+9%, $p=0.04$) in the Hypo bones (1.39±0.16, n=10) compared with the CTL bones (1.29±0.15, n=14). Comparing the two tracers within the same animal group using Student's *t*-tests, the transport enhancement of the larger tracer, parvalbumin, was higher than that of sodium fluorescein in both genotypes (CTL +8%, $p=0.08$; Hypo +10%, $p=0.04$, Fig. 2).

Solute Velocities

Using the genotype-specific three-compartment LCS models constructed for the Hypo and CTL bones, the transport enhancements (k/k_0) for sodium fluorescein and parvalbumin were obtained for various solute velocities v_s (0–80.6μm/s) through computer simulations (Fig. 3). The results for the four experimental groups (two tracer types and two genotypes) fit well with power relationships:

$$\text{Sodium fluorescein in the CTL bone:}\quad k/k_0=1+1.514\times10^{-4}\times {v_s}^{1.814}\ (R^2=0.99); \quad \text{(Eq. 4)}$$

$$\text{Parvalbumin in the CTL bone:}\quad k/k_0=1+2.888\times10^{-4}\times {v_s}^{1.784}\ (R^2=0.99); \quad \text{(Eq. 5)}$$

$$\text{Sodium fluorescein in the Hypo bone:} \quad k/k_0 = 1 + 0.985 \times 10^{-4} \times v_s^{1.847} \ (R^2 = 0.99); \quad \text{(Eq. 6)}$$

$$\text{Parvalbumin in the Hypo bone:} \quad k/k_0 = 1 + 1.820 \times 10^{-4} \times v_s^{1.815} \ (R^2 = 0.99). \quad \text{(Eq. 7)}$$

For a given solute velocity, the transport enhancement is inversely related to the solute diffusivity. The magnitudes of transport enhancement are thus ordered (from the least to highest) as sodium fluorescein in Hypo LCS, sodium fluorescein in CTL LCS, parvalbumin in Hypo LCS, and parvalbumin in CTL LCS (Fig. 3). From these relationships, the solute velocities giving rise to the mean transport enhancement measured within the four groups, as well as the range of velocities corresponding to one standard deviation above and below the mean transport enhancement were readily obtained (Table 3). On average, the current loading condition (3N peak loads at 0.5Hz with 4s resting periods) resulted in a peak velocity of 51.1μm/s and 48.2μm/s in the canaliculi of the CTL bones for sodium fluorescein and parvalbumin, respectively. However, in Hypo LCS, the same loading conditions resulted in a +39% and +42% increase in the peak velocity for sodium fluorescein (71.2μm/s) and parvalbumin (68.4μm/s), respectively.

Reflection Coefficient in the PCM

Due to its small Stokes radius and negligible reflection coefficient (~0.5%) within the osteocytic PCM (30), the velocity of sodium fluorescein was assumed to be that of the fluid velocity (v_f). The reflection coefficient of parvalbumin ($\sigma_f = 1 - v_s/v_f$) through the osteocytic PCM in the CTL and Hypo bones was therefore found to be 5.7% and 3.9%, respectively (Table 4), demonstrating an aging-related decrease in the 12–13 month-old CTL (−32.1%) and Hypo (−31.6%) mice, compared with that of the 4–5 month-old CTL young mice measured in our previous study ($\sigma_f = 8.4\%$) (30).

Osteocytic PCM Ultrastructure in the Canaliculi

Using our newly published PCM sieving model (30), possible configurations of PCM fiber matrix that could account for the observed reflection coefficients were estimated (Tables 5 and 6). Depending on the fiber radius (0.5–4nm), the fiber volume fraction varied in the ranges of 0.4%–17.2%, 0.2%–13.0%, and 0.1%–9.5% for the young 4–5 month-old bones, aged 12–13 month-old bones, and 12–13 month-old perlecan deficient bones, respectively (Table 5). For all the fiber sizes considered, a decrease in the fiber volume fraction ranging from −50% to −24% was clearly seen in the aged versus young bones. A similar degree of decrease in the fiber volume fraction (−50% to −27%) was observed in the Hypo versus age-matched control bones (Table 5). For an idealized square array of fibers, the effective fiber edge-to-edge spacing varied with fiber radius and among groups (Table 6). For the fiber radii considered (0.5nm–4nm), the fiber spacing varied from 12.9nm–9.1nm, 17.3nm–11.7nm, and 23.1nm–15.0nm for the young CTL, aged CTL, and aged-matched Hypo bones. Regardless of the radius assumed for the PCM fibers, the fiber spacing was consistently larger in the aged bones relative to the young bones (+34% to +29%) and in the Hypo bones relative to the CTL bones (+34% to +28%, Table 6).

Cellular-Level Mechanical Stimulations

Knowledge of the fiber spacing of the PCM fibers in the canaliculi allowed us to derive the detailed spatial profiles for the fluid flow in the CTL and Hypo bones under 3N peak load (Fig. 4). For the case of fiber radius of 2nm, the spatial velocity profile across the radial gap between the cell process and the canalicular wall followed a plug flow-like pattern in the CTL bones where the fiber spacing was 13.4nm (Table 6). However, the flow profile

became more parabolic-like in the Hypo bones where the fiber spacing was increased to 17.4nm for PCM fibers of the same radius of 2nm (Table 6). The peak fluid velocity was higher in the Hypo bones (99.7μm/s) than that predicted in the CTL bones (67.8μm/s). For the Hypo bones, the increased peak velocity and the narrower fluid annular gap (78nm vs. 87nm) resulted in a higher shear stress (as shown by a steeper slope) at the locations of the cell process membranes (CTL: r=74nm; Hypo: r=67nm). The fluid shear stress on the cell process membrane and the shearing force per unit length of the cell process were +34% and +24% increased, respectively, in the Hypo bones relative to CTL bones (Table 7). However, due to the reduced fiber density, the fluid drag force and the ratio of the fluid drag over the shearing force were reduced −35% and −48%, respectively, in the Hypo bones compared with the CTL bones (Table 7). Similar findings were found with three other fiber radii (0.5, 1, and 4nm) (data not shown).

Responses to *In Vivo* Loading

The non-loaded tibiae did not show significant differences in cortical μCT parameters between CTL and Hypo mice, except for a slightly higher tissue mineral density (Ct.TMD) in the Hypo mice (Table 1S). Loading resulted in an increase in cortical bone polar moment inertia (Ct.pMOI, +6.5%, p=0.02, Fig. 5A) and a reduction in the cortical porosity (−3.1%, p=0.04, Table 1S) in CTL mice, while no such anabolic effects were seen in the Hypo mice. Loading also significantly increased tibial stiffness in CTL mice (p=0.01), but did not increase the stiffness of Hypo tibiae (p=0.19, Fig. 5B). Dynamic bone labeling analysis revealed no difference in the mineralizing surface (MS/BS), mineral apposition rate (MAR), and bone formation rate (BFR/BS) in the non-loaded tibiae at either periosteal or endosteal surfaces (Table 1S). Loading did not significantly increase the Ps.MS/BS (Fig. C) but significantly increased Ps.MAR (+75%, p=0.03, Fig. 5D), resulting in an increase in Ps.BFR/BS (+141%, p=0.02, Table 1S) in CTL mice, while no such effects were detected, perhaps due to relatively larger data variability in the Hypo mice. Loading did not affect any of the endosteal measures (Table 1S). Overall, the preliminary data suggested diminished anabolic response to mechanical loading in the Hypo mice compared with the CTL mice.

Discussion

Although the osteocytic PCM, the critical interface between outer cell membrane and canalicular wall, is believed to play a key role in osteocyte nutrition, cell-to-cell signaling, and mechanosensing (13,15,34,36), there has been few quantitative studies characterizing its functions due to its small dimensions, its inaccessibility, and a lack of proper investigative tools. Using our recently developed tracer velocimetric approach (30), which combined FRAP-based confocal imaging and a hydrodynamic sieving model, we were able to study the effects of alterations in the osteocytic PCM, particularly loss of perlecan/HSPG2, on solute transport and fluid flow. We found increased diffusion and convection of both small and large molecules in cortical bone when the osteocytic PCM became sparser (Figs. 1 and 2). The perlecan-deficient mice used in this study represent a well-established model (27), in which the normal expression of perlecan, a large proteoglycan normally found in the osteocytic LCS, is genetically altered, similar to that in human SJS with profound musculoskeletal impairments (27,28). We found that a moderate mechanical loading (~300με) resulted in a significant fluid flow in normal bone (51.1μm/s), which was further elevated in the perlecan-deficient bone (71.2μm/s, Table 3). More importantly, we successfully detected changes in the sieving properties and the ultrastructure of the osteocytic PCM among young adult, aged, and perlecan-deficient bones (Tables 4–6), which allowed us to obtain detailed velocity profiles within their canalicular channels (Fig. 4), and the levels of mechanical stimulation forces such as the shear stress and fluid drag experienced by osteocytes *in situ* (Table 7). This study demonstrated that our FRAP-based

approach is sensitive enough to detect alterations in the osteocytic PCM density associated with aging and changes in specific PCM components. This study provides a solid foundation and a powerful tool for better characterizing the osteocytic PCM and dissecting its functional roles in bone physiology and pathology.

Validation of the tracer velocimetry approach

As discussed in our previous studies (30), the novelty of the approach lies on its capability of quantifying the sieving and structural properties (*i.e.*, reflection coefficient, fiber volume fraction, and fiber spacing) of the osteocytic PCM fibers, which are beyond the diffraction limited resolution of light microscopy (~0.2μm). This is accomplished by measuring the fiber-tracer interactions, which become measurable due to the collective draining of the flows inside the 50–100 discrete PCM-containing canalicular channels into the central photobleached lacuna (30). To the best of our knowledge there exist no studies directly measuring the PCM fiber volume fraction and few data on fiber spacing with which to directly compare our findings. Alternatively, we first checked the consistency of our results with previously published tracer perfusion data, followed by analysis of solute transport behaviors in the transgenic perlecan hypomorph mice, a model with known alterations in the PCM composition (27,28). Various-sized tracers have been perfused in living bone and their spatial distributions observed in histological sections (20,21,40). It was observed that molecules less than 6nm in diameter (such as procion red, horseradish peroxidase, 10 kDa dextran) could penetrate into the LCS, while larger molecules such as ferritin (12nm) and 60kDa dextran were excluded from the LCS (20,21,40). These studies suggest that the effective pore size of adult osteocyte PCM is between 6–12nm. In this study, we found that the fiber spacing in young adult bone ranged from 9.1nm to 12.9nm, depending on the individual fiber radius (Table 6). This result agreed with previous perfusion results very well. Second, our results demonstrated increased diffusion (Fig. 1) and convection (Table 3) of both small and large tracers in the perlecan-deficient bone, consistent with the prediction of a sparser PCM, which have been implied in this mouse model due to a reduction in perlecan protein expression and decreased number of tethering elements per canaliculus relative to the controls (27,28). Specifically, we identified an approximately 30% increase in the fiber spacing in the perlecan-deficient PCM compared with the age-matched wide type PCM. These agreements support the fidelity of our current approach in quantifying the osteocytic PCM.

Plug-flow vs. parabolic flow

Quantification of the fiber spacing values in various bones also allowed us to obtain the spatial velocity profiles of the load-induced canalicular fluid flows. Weinbaum and coworkers (13) predicted a Darcy-like (plug) flow through GAG-filled canaliculi assuming a fiber spacing of 7nm. This plug-flow pattern has been widely used in later studies (41). The fiber spacing measured in the 12–13 month-old CTL and Hypo bones was in the range of 11.7nm to 23nm. Fitting our measured fluid velocity and the fiber spacing values (13.4nm and 17.4nm in the case of 2nm fiber radius) into the Brinkman equation, we found that the flow velocity profile approximated a Darcy-like plug-flow in the CTL canaliculus, especially in the central lumen region, while flow shifted to a more parabolic-like waveform in the Hypo canaliculus due to an increased fiber spacing (Fig. 4). This result demonstrated that the local fluid velocity field in the PCM is quite sensitive to the density of the PCM fibers.

Shear stress vs. fluid drag

One fundamental question regarding osteocyte mechanotransduction is which physical signal(s) are sensed by osteocytes *in situ* and eventually lead to *in vivo* bone adaptation

processes (42). Both fluid shear stress acting on the cell membrane and fluid drag force acting on the tethering PCM fibers have been proposed for osteocytes (13,15). Osteocytes subjected to fluid shear stress in parallel-plate chambers have demonstrated both short-term responses (*e.g*., intracellular calcium signaling, and ATP, nitric oxide, and PGE_2 release) and long-term responses (*e.g*., expression of sclerostin, RANKL/OPG, as well as apoptosis) (2,18,43). However, very few experiments have been performed to investigate fluid drag via PCM. In one example, the PCM surrounding the MLO-Y4 cells was disrupted with hyaluronidase treatment and the flow-induced PGE_2 release was found to be completely abolished (44). In a recent study, MLO-Y4 cell processes were allowed to penetrate into microscopic channels inside a filter membrane to establish a semi 3D contact between cell process and surrounding matrix. Similarly, hyaluronidase treatment was found to block mechanically activated opening of connexin43 hemichannels (45), a critical step in the release of ATP and PGE2 in response to mechanical stimulation (46). These *in vitro* systems, although provide valuable insights on the PCM's role in osteocyte mechanotransduction, are not ideal for assessing relative contributions of the fluid shear stress versus fluid drag force to osteocyte mechanotransduction, largely owing to their lack of 3D cell-PCM interactions and LCS pore system observed *in vivo*. The analysis from the present study (Table 7) clearly demonstrates that we can dissect the roles of shear stress and fluid drag *in vivo* by using the perlecan-deficient model. Comparing the Hypo and CTL bones under the same mechanical loading (3N), osteocytes in the Hypo bones are anticipated to experience larger shearing force (+24%), but smaller fluid drag force (−35%) than those in the CTL bones (Table 7). The ratio between the drag force and the fluid shearing force is predicted to decrease by −48% in the Hypo bones compared with CTL bones. Therefore, the perlecan Hypo mouse can be used to test the relative contribution of shear stress and fluid drag during the *in vivo* bone adaptation process because the behaviors of shear stress and fluid drag are diverging under mechanical stimulation. If the shear stress is the primary signal that triggers osteocyte mechanotransduction, the Hypo mice are expected to respond to mechanical loading more rigorously than the CTL mice. On the other hand, if the fluid drag force is the triggering signal, the CTL mice are expected to be more responsive to loading. The latter case was supported by our preliminary *in vivo* loading data (47). We showed that tibial axial compressive loading (8.5N peak load at 4 Hz, 5 min per session, 5 sessions over a total of 10 days) significantly increased the stiffness and polar moment inertia in the loaded tibiae in the CTL mice by elevating the mineral apposition rate and bone formation rate (Fig. 5, Table 1S); in contrast, no significant anabolic changes were detected in the perlecan-deficient mice. These results suggest that bone adaptation is likely driven by fluid drag acting on the PCM fibers, but not shear stress acting on the osteocyte cell process membrane. However, it is noted that data variability in the perlecan deficient mice was greater than that in control mice. Therefore, future experiments with a larger sample size and/or a greater mechanical stimulation are needed to confirm the present results.

PCM fibers as osteocyte's "sensing antenna"

Our current data support the strain amplification hypothesis originally proposed by You et al. (2001) (15) and later refined by Han et al. (2004) (48) and Wang et al. (2007) (16). In contrast to Weinbaum's 1994 shear stress model (13), the strain amplification model assumed that the osteocytic PCM fibers tethering the canalicular wall and cell process are deformed by the fluid drag from the load-induced fluid flow. Tethering fibers have been visualized in TEM studies and the spacing of the tethering fiber was measured to be ~40nm (3), which was approximately three to four times larger than the fiber spacing (9–13nm) reported here for young adult bone (Table 6). It was likely that some tethering fibers were collapsed or lost during the TEM processing procedures. The chemical composition and mechanical strength of these tethering elements remain largely unknown, besides the

identification of extracellular perlecan inside the canaliculi in our recent study (27). From structural and mechanical points of view, perlecan is a highly viable candidate for mechanosensitive tethers, which need to form stable associations both with the cell membrane and the bone matrix lining the canalicular wall (Fig. 6). It is well established that perlecan, with five independently functioning domains (49), interacts with numerous ECM proteins (including those found in bone matrix), binds many growth factors, cytokines, and various transmembrane proteins (including integrins) at the cell surface (49,50). It is also possible that some PCM fibers are anchored only at one end, such as at the cell process membrane, with the other end possibly just touching the canalicular wall without being rigidly fixed to the wall. In this single-end anchorage configuration, the PCM fibers could still capture fluid drag, similarly to the way that endothelial glycocalyx interacts with blood flow. Conceptually, the single-end anchored PCM fibers, acting as sensing antenna, may be more compatible with motile osteocytic cell processes observed for newly embedded osteocytes (51). We are currently investigating perlecan's interactions with molecules associated with cell membrane and bone matrix.

PCM fiber density as an indicator of mechanosensitivity

Because the load-induced cellular stimulation forces are sensitive to the PCM fiber density (Table 7), we speculate that the PCM fiber density serves as an indicator/regulator of osteocyte's mechanosensitivity. Two lines of experiments support this hypothesis. First, in our *in vivo* loading study, perlecan-deficient mice (with a sparser PCM) failed to respond to mechanical loading that induced anabolic bone formation in control mice (with a denser PCM) (Fig. 5 and Table 1S), demonstrating an association between the PCM fiber density and bone's mechanosensitivity. Second, we detected a 29% to 34% decrease in PCM fiber density in the 12–13 month-old CTL bones compared with the 4–5 month-old CTL bones (Table 6). Data from the literature have demonstrated a diminishing mechanosensitivity in bone with aging (52,53), again supporting a potential association between the PCM fiber density and bone's mechanosensitivity. Because the synthesis of heparan sulfate proteoglycans does not change with aging (54), this age-related loss of PCM fibers is likely due to increased PCM shedding caused by accumulated oxidative stress in aging cells, as has been shown for the endothelial glycocalyx (55,56). Taken together, the existing evidence leads us to hypothesize that i) the PCM fibers act as the osteocyte's sensing antenna, capturing flow-induced fluid drag and transmitting this mechanical signal to the intracellular domain, and that ii) PCM fiber density influences bone's mechanosensitivity and *in vivo* bone adaptation to loading (Fig. 6). Within the range of the PCM fiber spacing (9–23nm) found herein, a denser PCM would result in a higher fluid drag force on the transverse fibers, which could trigger downstream signaling and/or gene expression processes. This could occur through actions that either modulate the opening or closing of transmembrane ion channels and hemichannels (for signaling with small secondary messengers such as Ca^{2+}, PGE_2, and ATP), or directly disturb the physically interconnected system consisting of PCM-integrin/focal adhesion complexes-cytoskeleton. Conversely, a sparser PCM would result in a reduction in fluid drag and a decrease in the degree of downstream responses in spite of similar mechanical loading at the whole bone level. Rigorous testing of this hypothesis calls for studies at the tissue, cellular, and molecular levels.

Limitations of the present studies

The present investigation adopted the one-color FRAP velocimetry approach as reported in our previous study (30) and thus suffered similar limitations. The main drawback was that the two fluid/solute tracking tracers were injected into separate sets of mice, introducing errors associated with inter-sample and inter-test variability. Because of this limitation, the reflection coefficient reported herein was obtained using the mean transport and anatomical values for a given genotype. We are currently developing a two-color imaging approach

where both probes (with distinct emission wavelengths) are injected into a single mouse to simultaneously measure fluid and solute velocities (57). Second, our hydrodynamic sieving model was limited to highly idealized fiber orientations, a single fiber species, and rigid, stationary fibers. These idealizations were made to obtain a closed-form solution to the problem. The more frequently observed radial transverse fibers within the canaliculi justified the assumption of the fiber arrays chosen in this model. As shown in our results (Table 6), the model-predicted edge-to-edge fiber spacing remains relatively constant regardless of the fiber radius, suggesting that this simple model succeeds in capturing the physics of the sieving properties of the PCM, which depends mainly on the effective fiber spacing. Third, because our previous TEM characterization of LCS anatomical parameters was performed in relatively old perlecan mice (8–9 months), the present study utilized 12–13 month-old perlecan deficient mice and the age-matched normal controls to validate the tracer velocimetry approach. Although they are excellent models for aged osteoporosis, we are aware that most *in vivo* loading studies, including our *in vivo* loading studies, used younger animals; we plan to map the changes of the PCM as a function of age in order to better correlate the studies of PCM structure to those of bone adaptation. Last, the perlecan deficiency in our Hypo mice affects not only bone but also other systems. It would be great to use transgenic models with bone-specific PCM alterations and/or on-demand initiation of PCM alteration. Because the perlecan/HSPG2 gene is a complex gene involved in many developmental processes (49,58), knockout mutation is lethal (59) and conditional bone-specific perlecan knockout models have yet to be developed. The current model is by far the best available model and the results are relevant to SJS patients (28,31,59,60).

Conclusions

We discovered that the FRAP tracer velocimetry approach was sensitive enough to detect i) the increases of fluid (+39%) and solute (+42%) convection through the LCS due to perlecan deficiency in 12–13 month-old murine tibiae under 3N and 0.5 Hz loading, and ii) the decreases in PCM fiber density associated with aging (from −29% to −34%) and perlecan deficiency (from −28% to −34%). PCM fiber spacing was found to be 9.1nm–12.9nm, 11.7nm–17.3nm, and 15.0–23.1nm for 4–5 month-old tibiae, 12–13 month-old tibiae, and 12–13 month-old perlecan deficient tibiae, respectively. This new knowledge allowed us, for the first time, to obtain the velocity profiles of the load-induced flow through the LCS and to predict the magnitude of flow-induced cell stimulation forces, such as shear stress and fluid drag. Decreased perlecan and PCM fiber density in the Hypo bone was found to increase fluid velocity (+34%) on the cell process membrane, but decreased fluid drag force per unit length of canaliculi (−35%), and a much reduced ratio of fluid drag force over shear force (−48%). When subjected to tibial axial loading (8.5N, 4Hz, 5min/session, 5 sessions over 10 days) in a preliminary in vivo experiment, 3.5-month-old Hypo mice did not respond to the anabolic stimuli as did normal CTL mice, supporting the idea that fibers in the PCM act as osteocyte's sensing antennae and that bone's mechanosensitivity depends on the PCM fiber density. If proven true in future studies, the PCM fiber density could be used to provide new targets to treat osteoporosis by modulating bone's intrinsic sensitivity to mechanical loading and to guide designs of patient-specific exercise regimens to promote bone formation.

Supplementary Material

Refer to Web version on PubMed Central for supplementary material.

Acknowledgments

Funding sources:

NIH (AR054385, AR064133; P20RR016458; P30GM103333; P01CA098912; P30AR050950)

China CSC Scholarship

The Fundamental Research Funds for the Central Universities, China (CDJXS12232258)

A special thank to Dr. W. R. Thompson, who first suggested investigating solute transport in the perlecan deficient mice. He and Dr. Price planned the initial TEM characterization study during a lunch meeting, which was expanded to the current full-scale study. This illustrates the importance of interdisciplinary collaborations in solving complex biological problems. The study was supported by the following funds: AR054385 (LW) and P30GM103333 (LW, CP, CKS), AR064133 (WRT), P01CA098912 (MCFC), P30AR050950 (XSL), CDJXS12232258 and CSC Fellowship of China (BW).

References

1. Jilka RL, Weinstein RS, Parfitt AM, Manolagas SC. Quantifying osteoblast and osteocyte apoptosis: challenges and rewards. J Bone Miner Res. 2007; 22(10):1492–501. [PubMed: 17542686]
2. Bonewald LF. The amazing osteocyte. J Bone Miner Res. 2011; 26(2):229–38. [PubMed: 21254230]
3. You LD, Weinbaum S, Cowin SC, Schaffler MB. Ultrastructure of the osteocyte process and its pericellular matrix. Anat Rec A Discov Mol Cell Evol Biol. 2004; 278(2):505–13. [PubMed: 15164337]
4. Roseman S. Reflections on glycobiology. J Biol Chem. 2001; 276(45):41527–42. [PubMed: 11553646]
5. Reitsma S, Slaaf DW, Vink H, van Zandvoort MA, oude Egbrink MG. The endothelial glycocalyx: composition, functions, and visualization. Pflugers Arch. 2007; 454(3):345–59. [PubMed: 17256154]
6. Frey A, Giannasca KT, Weltzin R, Giannasca PJ, Reggio H, Lencer WI, Neutra MR. Role of the glycocalyx in regulating access of microparticles to apical plasma membranes of intestinal epithelial cells: implications for microbial attachment and oral vaccine targeting. J Exp Med. 1996; 184(3): 1045–59. [PubMed: 9064322]
7. Chang J, Poole CA. Confocal analysis of the molecular heterogeneity in the pericellular microenvironment produced by adult canine chondrocytes cultured in agarose gel. Histochem J. 1997; 29(7):515–28. [PubMed: 9279554]
8. Weinbaum S, Zhang X, Han Y, Vink H, Cowin SC. Mechanotransduction and flow across the endothelial glycocalyx. Proc Natl Acad Sci U S A. 2003; 100(13):7988–95. [PubMed: 12810946]
9. Vincent TL, McLean CJ, Full LE, Peston D, Saklatvala J. FGF-2 is bound to perlecan in the pericellular matrix of articular cartilage, where it acts as a chondrocyte mechanotransducer. Osteoarthritis Cartilage. 2007; 15(7):752–63. [PubMed: 17368052]
10. Wilusz RE, Defrate LE, Guilak F. A biomechanical role for perlecan in the pericellular matrix of articular cartilage. Matrix Biol. 2012; 31(6):320–7. [PubMed: 22659389]
11. Piekarski K, Munro M. Transport mechanism operating between blood supply and osteocytes in long bones. Nature. 1977; 269(5623):80–2. [PubMed: 895891]
12. Price C, Zhou X, Li W, Wang L. Real-time measurement of solute transport within the lacunar-canalicular system of mechanically loaded bone: direct evidence for load-induced fluid flow. J Bone Miner Res. 2011; 26(2):277–85. [PubMed: 20715178]
13. Weinbaum S, Cowin SC, Zeng Y. A model for the excitation of osteocytes by mechanical loading-induced bone fluid shear stresses. J Biomech. 1994; 27(3):339–60. [PubMed: 8051194]
14. Cowin SC, Moss-Salentijn L, Moss ML. Candidates for the mechanosensory system in bone. J Biomech Eng. 1991; 113(2):191–7. [PubMed: 1875693]
15. You L, Cowin SC, Schaffler MB, Weinbaum S. A model for strain amplification in the actin cytoskeleton of osteocytes due to fluid drag on pericellular matrix. J Biomech. 2001; 34(11):1375–86. [PubMed: 11672712]
16. Wang Y, McNamara LM, Schaffler MB, Weinbaum S. A model for the role of integrins in flow induced mechanotransduction in osteocytes. Proc Natl Acad Sci U S A. 2007; 104(40):15941–6. [PubMed: 17895377]

17. McNamara LM, Majeska RJ, Weinbaum S, Friedrich V, Schaffler MB. Attachment of osteocyte cell processes to the bone matrix. Anat Rec (Hoboken). 2009; 292(3):355–63. [PubMed: 19248169]
18. Duncan RL, Turner CH. Mechanotransduction and the functional response of bone to mechanical strain. Calcif Tissue Int. 1995; 57(5):344–58. [PubMed: 8564797]
19. Thompson WR, Majid AS, Czymmek KJ, Ruff AL, Garcia J, Duncan RL, Farach-Carson MC. Association of the alpha(2)delta(1) subunit with Ca(v)3.2 enhances membrane expression and regulates mechanically induced ATP release in MLO-Y4 osteocytes. J Bone Miner Res. 2011; 26(9):2125–39. [PubMed: 21638318]
20. Tami AE, Schaffler MB, Knothe Tate ML. Probing the tissue to subcellular level structure underlying bone's molecular sieving function. Biorheology. 2003; 40(6):577–90. [PubMed: 14610309]
21. Wang L, Ciani C, Doty SB, Fritton SP. Delineating bone's interstitial fluid pathway in vivo. Bone. 2004; 34(3):499–509. [PubMed: 15003797]
22. Li W, You L, Schaffler MB, Wang L. The dependency of solute diffusion on molecular weight and shape in intact bone. Bone. 2009; 45(5):1017–23. [PubMed: 19647808]
23. Sauren YM, Mieremet RH, Groot CG, Scherft JP. An electron microscopic study on the presence of proteoglycans in the mineralized matrix of rat and human compact lamellar bone. Anat Rec. 1992; 232(1):36–44. [PubMed: 1536463]
24. Shapiro F, Cahill C, Malatantis G, Nayak RC. Transmission electron microscopic demonstration of vimentin in rat osteoblast and osteocyte cell bodies and processes using the immunogold technique. Anat Rec. 1995; 241(1):39–48. [PubMed: 7879923]
25. Hunziker EB, Herrmann W, Schenk RK. Improved cartilage fixation by ruthenium hexammine trichloride (RHT). A prerequisite for morphometry in growth cartilage. J Ultrastruct Res. 1982; 81(1):1–12. [PubMed: 7143533]
26. Rostgaard J, Qvortrup K. Sieve plugs in fenestrae of glomerular capillaries--site of the filtration barrier? Cells Tissues Organs. 2002; 170(2–3):132–8. [PubMed: 11731701]
27. Thompson WR, Modla S, Grindel BJ, Czymmek KJ, Kirn-Safran CB, Wang L, Duncan RL, Farach-Carson MC. Perlecan/Hspg2 deficiency alters the pericellular space of the lacunocanalicular system surrounding osteocytic processes in cortical bone. J Bone Miner Res. 2011; 26(3):618–29. [PubMed: 20814969]
28. Rodgers KD, Sasaki T, Aszodi A, Jacenko O. Reduced perlecan in mice results in chondrodysplasia resembling Schwartz-Jampel syndrome. Hum Mol Genet. 2007; 16(5):515–28. [PubMed: 17213231]
29. Roberts IS, Gleadle JM. Familial nephropathy and multiple exostoses with exostosin-1 (EXT1) gene mutation. J Am Soc Nephrol. 2008; 19(3):450–3. [PubMed: 18216313]
30. Wang B, Zhou X, Price C, Li W, Pan J, Wang L. Quantifying load-induced solute transport and solute-matrix interaction within the osteocyte lacunar-canalicular system. J Bone Miner Res. 2013; 28(5):1075–86. [PubMed: 23109140]
31. Nicole S, Davoine CS, Topaloglu H, Cattolico L, Barral D, Beighton P, Hamida CB, Hammouda H, Cruaud C, White PS, Samson D, Urtizberea JA, Lehmann-Horn F, Weissenbach J, Hentati F, Fontaine B. Perlecan, the major proteoglycan of basement membranes, is altered in patients with Schwartz-Jampel syndrome (chondrodystrophic myotonia). Nat Genet. 2000; 26(4):480–3. [PubMed: 11101850]
32. Arikawa-Hirasawa E, Watanabe H, Takami H, Hassell JR, Yamada Y. Perlecan is essential for cartilage and cephalic development. Nat Genet. 1999; 23(3):354–8. [PubMed: 10545953]
33. Price C, Li W, Novotny JE, Wang L. An in-situ fluorescence-based optical extensometry system for imaging mechanically loaded bone. J Orthop Res. 2009
34. Wang L, Wang Y, Han Y, Henderson SC, Majeska RJ, Weinbaum S, Schaffler MB. In situ measurement of solute transport in the bone lacunar-canalicular system. Proc Natl Acad Sci U S A. 2005; 102(33):11911–6. [PubMed: 16087872]
35. McCreadie BR, Hollister SJ, Schaffler MB, Goldstein SA. Osteocyte lacuna size and shape in women with and without osteoporotic fracture. J Biomech. 2004; 37(4):563–72. [PubMed: 14996569]

36. Zhou X, Novotny JE, Wang L. Modeling fluorescence recovery after photobleaching in loaded bone: potential applications in measuring fluid and solute transport in the osteocytic lacunar-canalicular system. Ann Biomed Eng. 2008; 36(12):1961–77. [PubMed: 18810639]
37. Chen CH, Hansma HG. Basement membrane macromolecules: insights from atomic force microscopy. J Struct Biol. 2000; 131(1):44–55. [PubMed: 10945969]
38. Fritton JC, Myers ER, Wright TM, van der Meulen MC. Bone mass is preserved and cancellous architecture altered due to cyclic loading of the mouse tibia after orchidectomy. J Bone Miner Res. 2008; 23(5):663–71. [PubMed: 18433300]
39. Liu XS, Ardeshirpour L, VanHouten JN, Shane E, Wysolmerski JJ. Site-specific changes in bone microarchitecture, mineralization, and stiffness during lactation and after weaning in mice. J Bone Miner Res. 2012; 27(4):865–75. [PubMed: 22189918]
40. Knothe Tate ML, Niederer P, Knothe U. In vivo tracer transport through the lacunocanalicular system of rat bone in an environment devoid of mechanical loading. Bone. 1998; 22(2):107–17. [PubMed: 9477233]
41. Cowin SC. Bone poroelasticity. J Biomech. 1999; 32(3):217–38. [PubMed: 10093022]
42. Klein-Nulend J, Bakker AD, Bacabac RG, Vatsa A, Weinbaum S. Mechanosensation and transduction in osteocytes. Bone. 2013; 54(2):182–90. [PubMed: 23085083]
43. Riddle RC, Donahue HJ. From streaming-potentials to shear stress: 25 years of bone cell mechanotransduction. J Orthop Res. 2009; 27(2):143–9. [PubMed: 18683882]
44. Reilly GC, Haut TR, Yellowley CE, Donahue HJ, Jacobs CR. Fluid flow induced PGE2 release by bone cells is reduced by glycocalyx degradation whereas calcium signals are not. Biorheology. 2003; 40(6):591–603. [PubMed: 14610310]
45. Burra S, Nicolella DP, Francis WL, Freitas CJ, Mueschke NJ, Poole K, Jiang JX. Dendritic processes of osteocytes are mechanotransducers that induce the opening of hemichannels. Proc Natl Acad Sci U S A. 2010; 107(31):13648–53. [PubMed: 20643964]
46. Loiselle AE, Jiang JX, Donahue HJ. Gap junction and hemichannel functions in osteocytes. Bone. 2013; 54(2):205–12. [PubMed: 23069374]
47. Price, C.; Lai, X.; Quabili, T.; Tseng, W-J.; Liu, XS.; Kirn-Safran, C.; Wang, L. Osteocyte Pericellular Matrix Density Regulates Bone's Anabolic Response to Mechanical Loading. The 2013 Annual Meeting of the American Society of Bone and Mineral Research; Baltimore, MD. 2013.
48. Han Y, Cowin SC, Schaffler MB, Weinbaum S. Mechanotransduction and strain amplification in osteocyte cell processes. Proc Natl Acad Sci U S A. 2004; 101(47):16689–94. [PubMed: 15539460]
49. Farach-Carson MC, Carson DD. Perlecan--a multifunctional extracellular proteoglycan scaffold. Glycobiology. 2007; 17(9):897–905. [PubMed: 17442708]
50. Knox SM, Whitelock JM. Perlecan: how does one molecule do so many things? Cell Mol Life Sci. 2006; 63(21):2435–45. [PubMed: 16952056]
51. Veno PA, Nicolella DP, Kalajzic I, Rowe DW, Bonewald LF, Dallas SL. Dynamic Imaging in Living Calvaria Reveals the Motile Properties of Osteoblasts and Osteocytes and suggests Heterogeneity of Osteoblasts in Bone. J Bone Miner Res. 2007; 22(suppl 1):S13.
52. Lynch ME, Main RP, Xu Q, Schmicker TL, Schaffler MB, Wright TM, van der Meulen MC. Tibial compression is anabolic in the adult mouse skeleton despite reduced responsiveness with aging. Bone. 2011; 49(3):439–46. [PubMed: 21642027]
53. Turner CH, Takano Y, Owan I. Aging changes mechanical loading thresholds for bone formation in rats. J Bone Miner Res. 1995; 10(10):1544–9. [PubMed: 8686511]
54. Fedarko NS, Vetter UK, Weinstein S, Robey PG. Age-related changes in hyaluronan, proteoglycan, collagen, and osteonectin synthesis by human bone cells. J Cell Physiol. 1992; 151(2):215–27. [PubMed: 1572898]
55. Mulivor AW, Lipowsky HH. Inflammation- and ischemia-induced shedding of venular glycocalyx. Am J Physiol Heart Circ Physiol. 2004; 286(5):H1672–80. [PubMed: 14704229]
56. Marechal X, Favory R, Joulin O, Montaigne D, Hassoun S, Decoster B, Zerimech F, Neviere R. Endothelial glycocalyx damage during endotoxemia coincides with microcirculatory dysfunction and vascular oxidative stress. Shock. 2008; 29(5):572–6. [PubMed: 18414231]

57. Lai, X.; Price, C.; Wang, L. Feasibility Studies on In Situ Imaging-Based Quantification of the Density of Osteocyte Pericellular. Matrix The 2013 Annual Meeting of the American Society of Bone and Mineral Research; Baltimore, MD. 2013.

58. Melrose J, Smith S, Knox S, Whitelock J. Perlecan, the multidomain HS-proteoglycan of basement membranes, is a prominent pericellular component of ovine hypertrophic vertebral growth plate and cartilaginous endplate chondrocytes. Histochem Cell Biol. 2002; 118(4):269–80. [PubMed: 12376823]

59. Stum M, Davoine CS, Fontaine B, Nicole S. Schwartz-Jampel syndrome and perlecan deficiency. Acta Myol. 2005; 24(2):89–92. [PubMed: 16550923]

60. Arikawa-Hirasawa E, Le AH, Nishino I, Nonaka I, Ho NC, Francomano CA, Govindraj P, Hassell JR, Devaney JM, Spranger J, Stevenson RE, Iannaccone S, Dalakas MC, Yamada Y. Structural and functional mutations of the perlecan gene cause Schwartz-Jampel syndrome, with myotonic myopathy and chondrodysplasia. Am J Hum Genet. 2002; 70(5):1368–75. [PubMed: 11941538]

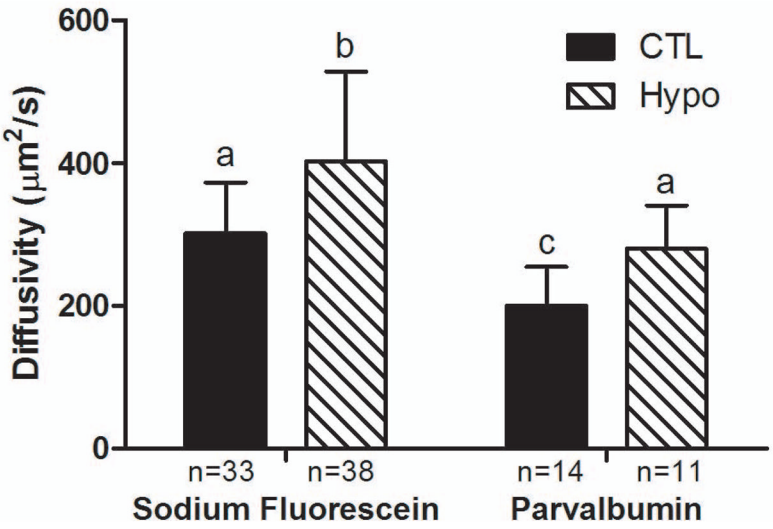

Figure 1.

Diffusivity of sodium fluorescein (Stokes radius 0.45nm) and parvalbumin (Stokes radius 1.31nm) in cortical bone LCS of the 12–13 month-old CTL and perlecan-deficient (Hypo) mice. Two-way ANOVA showed that genotype ($F_{1,92}$=16.4, $p<0.0001$) and tracer type ($F_{1,92}$=25.31, $p<0.0001$) had significant effects on the measurements. Perlecan deficiency increased diffusion for both small and large molecules. Bars denoted with different letters are significantly different in paired comparisons ($p<0.05$). The sample size (the number of lacunae subjected to FRAP tests) is indicated for each study group directly under the corresponding data.

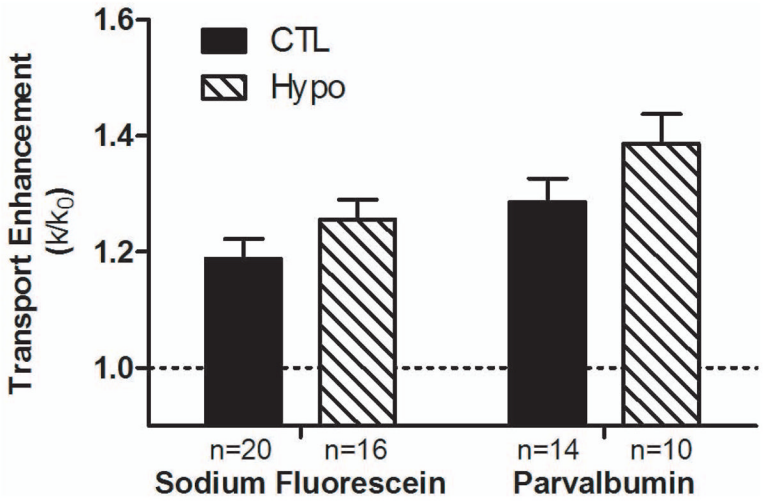

Figure 2.

Transport enhancement of sodium fluorescein and parvalbumin in loaded vs. non-loaded tibial LCS of the 12–13 month-old perlecan-deficient (Hypo) and control (CTL) mice. Two-way ANOVA showed that genotype ($F_{1,56}$=4.44, P=0.04) and tracer type ($F_{1,56}$=8.08, P=0.006) had significant effects on the measurements. Although no significant difference was detected for multiple comparison using Bonferroni *post hoc* tests, the larger parvalbumin moved significantly faster in the Hypo PCM relative to the CTL PCM as assessed by unpaired Student's *t*-test (p=0.03). N values of paired FRAP tests per study group ranged from 10–20 lacunae.

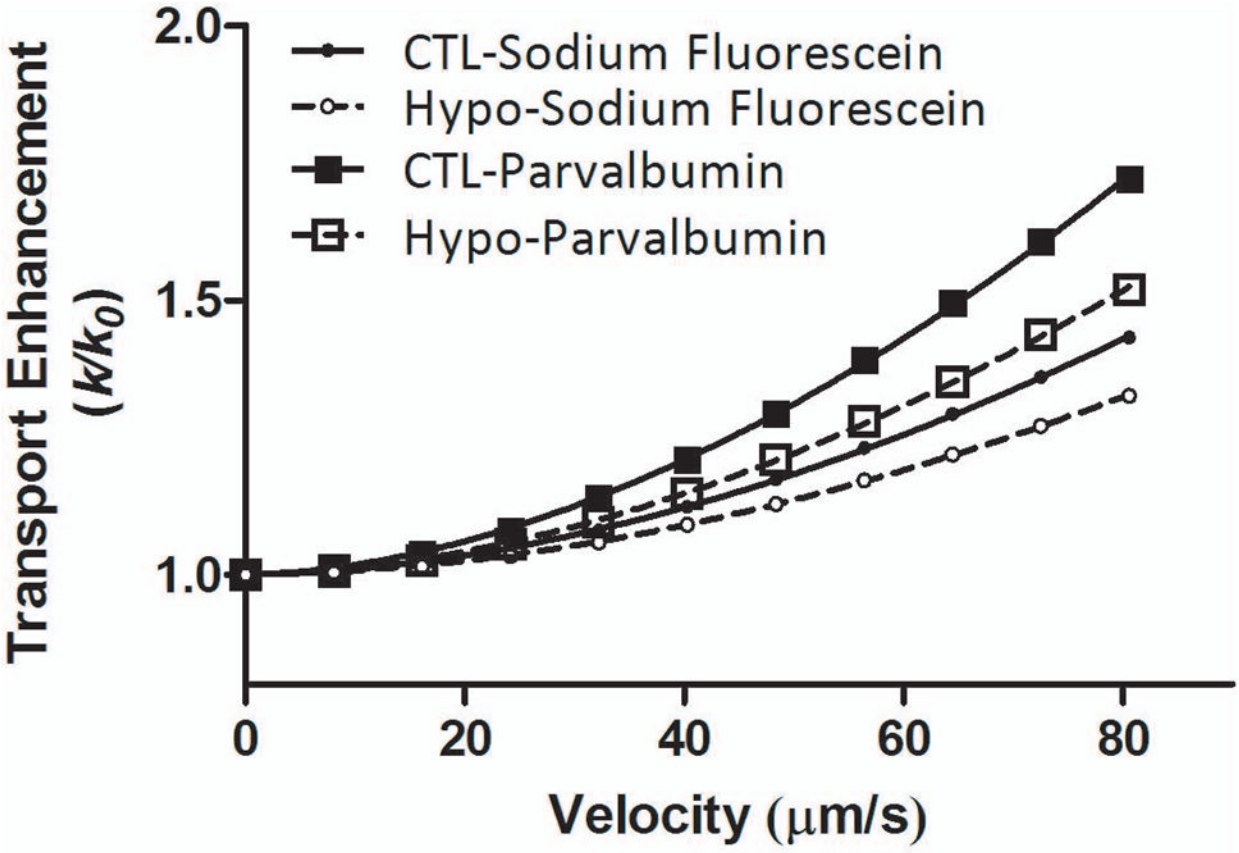

Figure 3.

Simulated transport enhancement as a function of solute velocity for the 12–13 month-old CTL and Hypo bone LCS, using their custom three-compartment transport models. The transport enhancement followed a power relationship with the solute velocity in both CTL (solid lines) and Hypo bones (dashed lines) and for sodium fluorescein (smaller circles) and parvalbumin (larger squares). Detailed relationships can be found in text (Equations 4–7). For a given solute velocity, the transport enhancement is inversely related to the solute diffusivity. The magnitudes of transport enhancement are thus ordered (from the least to highest) as sodium fluorescein in Hypo LCS, sodium fluorescein in CTL LCS, parvalbumin in Hypo LCS, and parvalbumin in CTL LCS.

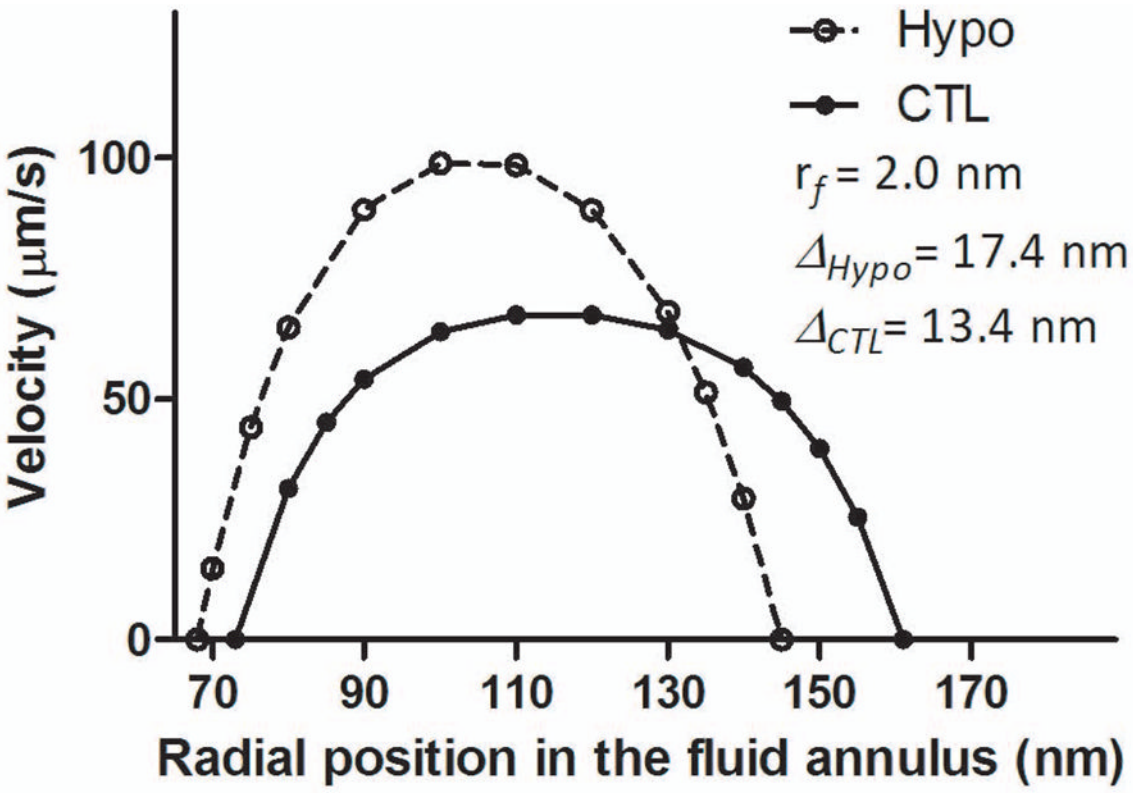

Figure 4.

Canalicular flow profiles for the 12–13 month-old CTL and Hypo bones under 3N peak load. For the case of fiber radius of 2nm, the velocity profile between the cell process and the canalicular wall appeared to be more plug flow-like in the CTL bones (the fiber spacing of 13.4nm) but more parabolic-like in the Hypo bones (the fiber spacing of 17.4nm). Note that the fluid annulus in the Hypo bones had a gap of 78nm between the cell process membrane at *r*=67nm and the canalicular wall at *r*=145nm, which was −10% smaller than that in the CTL bones (a gap of 87nm between the cell process membrane at *r*=74 nm and the canalicular wall at *r*=161nm) as reported in Table 1. Similar profiles were found for other cases of fiber radius (0.5, 1, and 4nm) with slight changes (<5%) in the peak velocities.

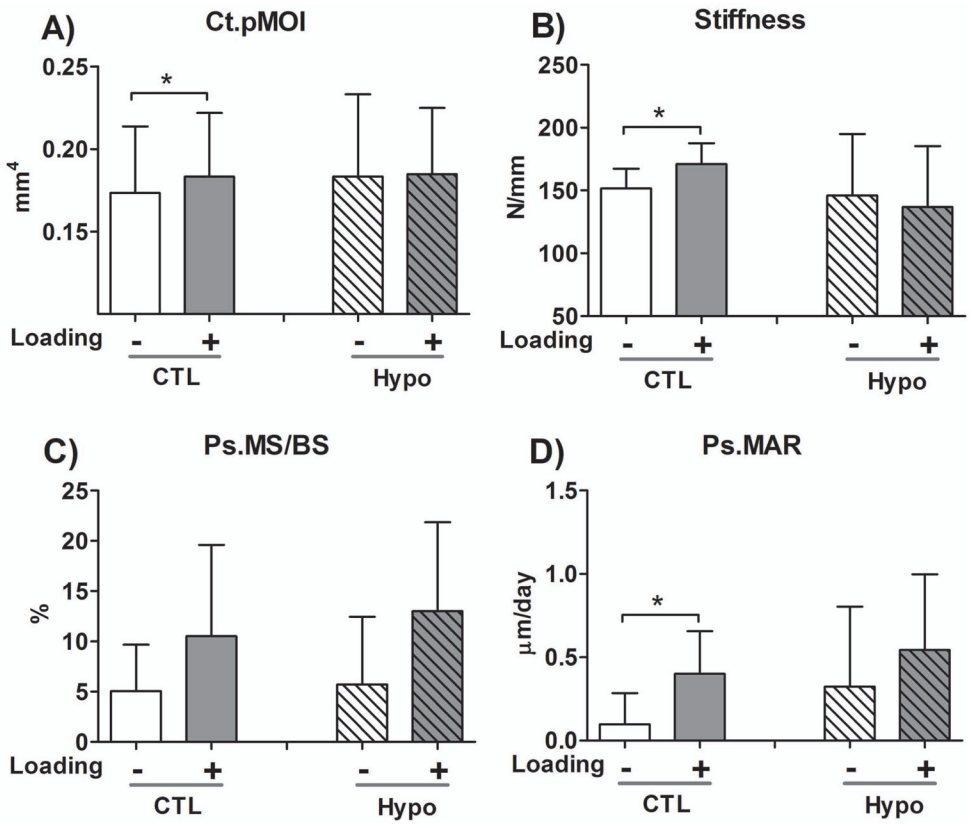

Figure 5.

The 3.5-month-old Hypo mice did not respond to anabolic tibial loading (8.5N peak load, 4 cycles/s, 5 min per session, 5 sessions over 10 days) as did the age-matched CTL mice in a preliminary experiment. (A) Cortical bone polar moment inertia (Ct.pMOI); (B) tibial stiffness; (C) Periosteal mineralizing surface (Ps.MS/BS); and (D) Periosteal mineral apposition rate (Ps.MAR). Sample sizes: N=8 CTL and N=6 Hypo mice for micro-CT analysis; N=7 CTL and N=6 Hypo mice for mechanical testing and bone labeling analyses. Despite the inter-animal variations within CTL or Hypo groups, Student's *t*-tests on the non-loaded vs. loaded paired tibiae revealed significant changes ($p<0.05$, denoted by * symbols) in CTL mice but not in Hypo mice. A full data set with other histomorphometry parameters and detailed *p* values of statistical tests can be found in Table 1S in the Supplementary Materials.

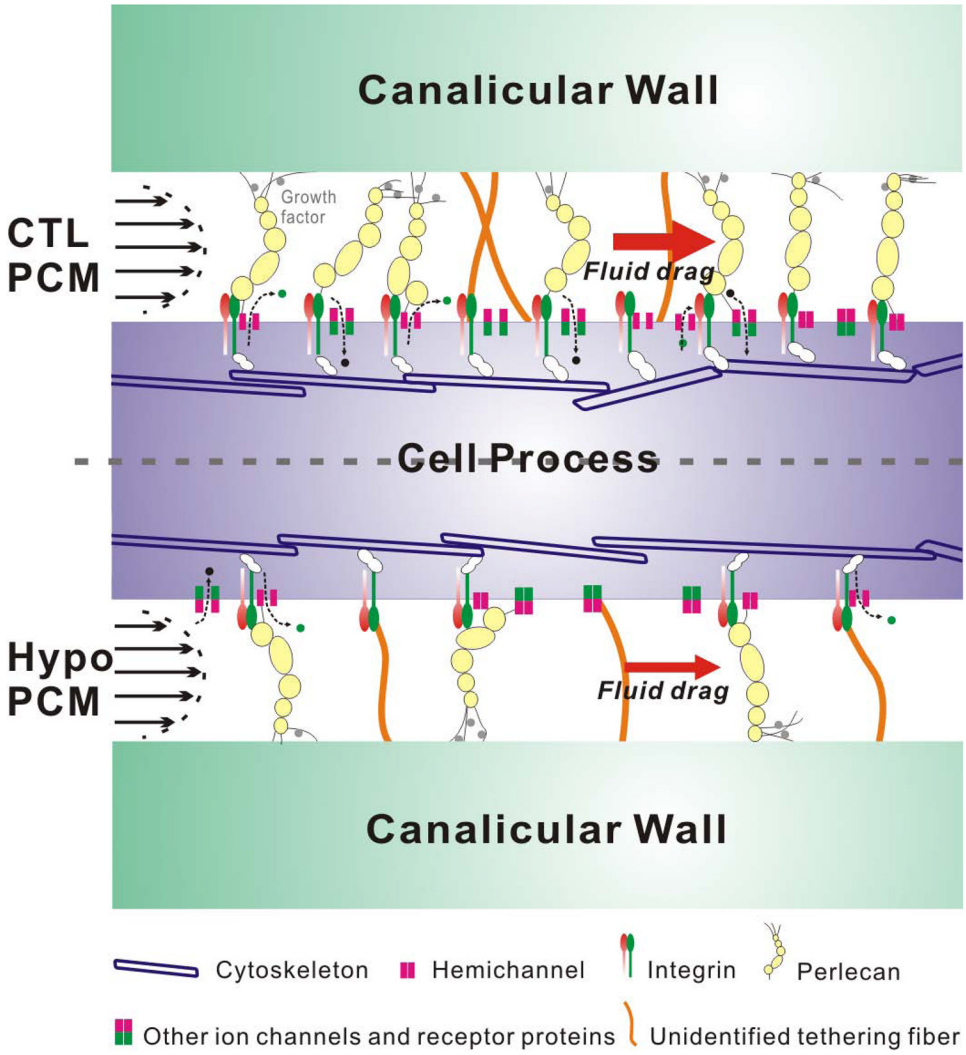

Figure 6.

A working hypothesis depicting the osteocytic perlecan-rich PCM, which act as flow-sensing antenna, capturing flow-induced fluid drag, and triggering osteocyte's mechanotransduction process. A denser PCM (as in normal CTL bone) would result in a higher fluid drag force on the transverse tethered fibers, which could trigger downstream signaling and/or gene expression through interactions with cell membrane via various channels, membrane receptors, or the physically connected PCM-integrin/focal adhesion complex-cytoskeleton system. Conversely, a sparser PCM (as in perlecan-deficient bone) would result in a smaller fluid drag and the degree of downstream responses would be reduced in spite of the same mechanical loading at the whole bone level.

Table 1

Confocal and TEM imaging of the LCS transport features in the 8–9 month-old male control (CTL) and perlecan deficient (Hypo) mice

Measurements	Control Bone (CTL)		Perlecan Deficient Bone (Hypo)		*p*-value
	Mean (±SD)	Sample Size	Mean (±SD)	Sample size	
Canalicular number density (#/μm^2)	0.21 (±0.05)	30 lacunae	0.19 (±0.02)	30 lacunae	<0.05
Canalicular wall cross-sectional area (μm^2)	0.081 (±0.001)	506 canaliculi	0.066 (±0.007)	475 canaliculi	<0.0001
Cell process cross-sectional area (μm^2)	0.017 (±0.002)	506 canaliculi	0.014 (±0.002)	475 canaliculi	0.0002
Canalicular fluid annular area (μm^2)	0.065 (±0.034)	506 canaliculi	0.053 (±0.026)	475 canaliculi	<0.0001
Lacunar fluid gap* (μm)	0.47 (±0.27)	12 lacunae	0.38 (±0.17)	16 lacunae	0.32

*Note: As there was no significant difference between the two groups, data were pooled, yielding a median value of 0.36 μm, which was used for the three-compartment modeling. Student's t-tests were performed for comparisons.

Table 2

Lacunar morphology in the 12–13 month-old male control (CTL) and perlecan deficient (Hypo) mice subjected to FRAP tests

Measurements	Control Bone (CTL, n=79 lacunae)	PCM Deficient Bone (Hypo, n=79 lacunae)	p-value
Lacunar projected area (*A*, μm^2)	97 (±22)	96 (±20)	0.7
Lacunar volume (*LacVol*, μm^3)	497 (±178)	492 (±166)	0.8
Lacunar surface area (*LacSurf*, μm^2)	329 (±75)	325 (±68)	0.7
Contributing canalicular number (*n*)	15.2 (±3.5)	13.6 (±2.8)	<0.003
Canalicular length (*d*, μm)	26.7 (±4.2)	30.3 (±5.2)	<0.0001
V_r (=*CanVol/LacVol*)*	0.056 (±0.01)	0.046 (±0.009)	<0.0001

* Note: V_r is the fluid volume ratio between the canaliculi and the sink lacuna (CanVol/LacVol); the CanVol is the product of the contributing canalicular number n, the canalicular annular area measured in TEM (Table 1), and the canalicular length d. Student's t-tests were performed for comparisons.

Table 3

Load-induced tracer velocity in the bone canaliculi of the 12–13 month-old male control (CTL) and perlecan deficient (Hypo)

Genotype	Age (Months)	Molecule	Loading Peak (N)	Solute velocity for mean TE (μm/s)	Velocity range for TE-SD to TE+SD (μm/s)
CTL	12–13	Sodium Fluorescein	3	51.1	21.6 – 70.4
		Parvalbumin	3	48.2	32.0 – 60.8
Hypo	12–13	Sodium Fluorescein	3	71.2	46.8 – 89.9
		Parvalbumin	3	68.4	51.2 – 82.7

Table 4

PCM's sieving property measured in young adult, aged CTL and aged Hypo bones using the FRAP tracer velocimetry approach

	Young bone	Aged CTL bone	Aged Hypo bone	Relative change (Aged vs. Young)	Relative change (Hypo vs. CTL)
Age (Months)	4–5	12–13	12–13		
Reflection Coefficient	8.4%*	5.7%	3.9%	−32.1%	−31.6%

*Note: measured in our previous study (30).

Table 5

Fiber volume fraction estimated for young adult, aged CTL and aged Hypo bones

Fiber radius* (nm)	Young bone	Aged CTL bone	Aged Hypo bone	Relative change (Aged vs. Young)	Relative change (Hypo vs. CTL)
0.5	0.4%	0.2%	0.1%	−50%	−50%
1	1.7%	1.1%	0.6%	−35%	−45%
2	6.1%	4.1%	2.7%	−33%	−34%
4	17.2%	13.0%	9.5%	−24%	−27%

* Note: Fiber radius was parametrically varied from 0.5 (size of GAG), 1–2nm (size of proteoglycan core proteins), to 4nm (repeated features in endothelial glycocalyx).

Table 6

Fiber spacing estimated for young adult, aged CTL and aged Hypo bones

Fiber radius (nm)	Young bone (nm)	Aged CTL bone (nm)	Aged Hypo bone (nm)	Relative change (Aged vs. Young)	Relative change (Hypo vs. CTL)
0.5	12.9	17.3	23.1	34%	34%
1	11.6	15.3	20.2	32%	32%
2	10.3	13.4	17.4	30%	30%
4	9.1	11.7	15.0	29%	28%

Table 7

Comparisons of fluid shear stress and drag force between aged CTL and Hypo bones under 3N tibial loading

	CTL Bone	Hypo Bone	Relative change (Hypo vs. CTL)
Shear stress on cell membrane (Pa)	5.9	7.9	+34%
Shearing force over 1μm cell process (pN)	2.72	3.38	+24%
Fluid drag force over 1μm cell process (pN)	18.4	12.0	−35%
Ratio of fluid drag over shearing force	6.8	3.5	−48%

Note: Both bones were loaded at 3N peak load at 0.5Hz; the fiber spacing for fibers in radius of 2nm was 13.4nm (CTL) and 17.4nm (Hypo), respectively (Table 6).